

Finite-amplitude method for collective inertia in spontaneous fissionKouhei Washiyama ^{1,*}, Nobuo Hinohara ^{2,3} and Takashi Nakatsukasa ^{2,3}¹*Research Center for Superheavy Elements, Kyushu University, Fukuoka 819-0395, Japan*²*Center for Computational Sciences, University of Tsukuba, Tsukuba 305-8577, Japan*³*Faculty of Pure and Applied Sciences, University of Tsukuba, Tsukuba 305-8571, Japan*

(Received 10 November 2020; accepted 14 December 2020; published 11 January 2021)

Background: Microscopic description of spontaneous fission is one of the most challenging subjects in nuclear physics. It is necessary to evaluate the collective potential and the collective inertia along a fission path for a description of quantum tunneling in spontaneous or low-energy fission. In past studies of the fission dynamics based on nuclear energy density functional (EDF) theory, the collective inertia has been evaluated with the cranking approximation, which neglects dynamical residual effects.

Purpose: The purpose is to provide a reliable and efficient method to include dynamical residual effects in the collective inertia for fission dynamics.

Methods: We use the local quasiparticle random-phase approximation (LQRPA) to evaluate the collective inertia along a fission path obtained by the constrained Hartree-Fock-Bogoliubov method with the Skyrme EDF. The finite-amplitude method (FAM) with a contour integration technique enables us to efficiently compute the collective inertia in a large model space.

Results: We evaluate the FAM-QRPA collective inertia along a symmetric fission path in ²⁴⁰Pu and ²⁵⁶Fm. The FAM-QRPA inertia is significantly larger than the one of the cranking approximation and shows pronounced peaks around the ground state and the fission isomer. This is due to dynamical residual effects.

Conclusions: To describe the spontaneous or low-energy fission, we provide a reliable and efficient method to construct the collective inertia with dynamical residual effects that have been neglected in most of EDF-based works in the past. We show the importance of dynamical residual effects to the collective inertia. This work will be a starting point for a systematic study of fission dynamics in heavy and superheavy nuclei to microscopically describe the nuclear large-amplitude collective motions.

DOI: [10.1103/PhysRevC.103.014306](https://doi.org/10.1103/PhysRevC.103.014306)**I. INTRODUCTION**

Nuclear fission [1–3] plays an important role in various phenomena such as synthesis of superheavy elements [4,5] and *r*-process nucleosynthesis in the universe [6–8]. The fission governs the existence and decay property of superheavy nuclei. Various types of fission, such as neutron-induced fission, spontaneous fission, and β -delayed fission that involve neutron-rich heavy and superheavy nuclei, are important in expected environment in the *r*-process.

Theoretically, a microscopic description of large-amplitude collective motions, such as nuclear fission and fusion, is one of the challenging subjects in quantum many-body physics. Of particular interest is quantum many-body tunneling for spontaneous or low-energy fission and subbarrier fusion of complex nuclei.

The most promising candidate for the microscopic approach is the self-consistent nuclear energy density functional (EDF) theory [9,10]. It is well established that the nuclear EDF gives a good description of ground-state properties of nuclei in the whole nuclear chart. The EDF approaches to the spontaneous fission have used a semiclassical description

with the Wenzel-Kramers-Brillouin (WKB) approximation for quantum tunneling. These studies show how the result depends on the choice of relevant collective variables, the collective potential energy, and the collective inertia entering the action integral in the WKB approximation. The potential energy has been calculated by the Hartree-Fock-Bogoliubov method with constraints on the collective variables. On the other hand, the collective inertia used in the previous EDF-based works [11–15] is insufficient in the following respect: First of all, the previous works employ the so-called cranking approximation to the adiabatic time-dependent Hartree-Fock-Bogoliubov (ATDHFB) method [16] to evaluate the collective inertia. The cranking approximation neglects dynamical residual effects, especially the time-odd terms of the EDF. This gives a big drawback, namely, the violation of the (local) Galilean symmetry, which leads to the incorrect total mass for the translational motion [10,17]. The rotational moments of inertia of deformed nuclei are not properly given in the cranking approximation [18]. In addition, the collective inertia of the cranking approximation significantly deviates from the one including the dynamical residual effects [19]. Irrespective of such drawbacks, because of its simplicity, the cranking approximation has been widely used in evaluating collective inertia not only for fission dynamics but also for the collective Hamiltonian method [20–24]. It should be noted that the

*washiyama@phys.kyushu-u.ac.jp

enhancement factors of 1.2–1.4 are often adopted to correct the missing residual effect.

An alternative method to ATDHFB for describing large-amplitude collective motions has been developed, called the adiabatic self-consistent collective coordinate (ASCC) method [25]. Based on the ASCC method, an efficient and feasible method to construct the collective Hamiltonian has been proposed [26]. In this method, the collective path (subspace) is determined by the constrained HFB (CHFb) calculation, while the collective inertia (the vibrational mass in the vibrational kinetic Hamiltonian) is determined by local normal modes built on CHFb states. Local normal modes are obtained by solving local quasiparticle random-phase approximation (LQRPA) equations. Dynamical residual effects with time-odd components are self-consistently included in the collective inertia by the LQRPA. This method, called CHFb + LQRPA, has been applied to constructing a five-dimensional quadrupole collective Hamiltonian for triaxial shapes with the pairing-plus-quadrupole (P + Q) Hamiltonian [26–29], a hybrid model of the P + Q Hamiltonian and covariant EDF [30], and three-dimensional quadrupole collective Hamiltonian for axially symmetric shapes with the Skyrme EDF [31]. Those works have shown the importance of including dynamical residual effects with time-odd components on the description of large-amplitude collective motion.

Despite much evidence for the importance of dynamical residual effects, no practical application based on the ATDHFB method takes into account residual effects in the calculation of the collective inertia. The reason is that it requires huge numerical computations to apply directly the ATDHFB (or LQRPA) formulas to the collective inertia in realistic cases, due to the size of the matrices treated with modern EDFs.

A method to efficiently solve the QRPA equations based on linear-response theory has been developed for the EDF, called the finite-amplitude method (FAM) [32]. In the FAM, response functions to an external one-body field can be obtained only with one-body induced densities and fields with an iterative scheme. The FAM requires matrices with the size of approximately $N \times N$, while the QRPA equation requires those with the size $\approx N^2 \times N^2$, where N represents the number of single-particle basis states. N may exceed 10^3 when, for example, 20 major shells in the harmonic-oscillator basis are used in solving deformed HFB equations. Thus, the computational cost of the FAM is significantly lower than that of QRPA. As an alternative way of solving the QRPA equations, the FAM has been employed in various applications [33–46].

The standard FAM formalism has been extended to the one in terms of the momentum–coordinate (PQ) representation [47] to treat zero-energy modes of QRPA solutions known as spurious modes or Nambu–Goldstone (NG) modes [48,49] associated with spontaneous symmetry breaking of the mean field. A general method to calculate the inertia of the NG modes was also given [47], which was applied to pairing rotation [50,51] and to spatial rotation of axially deformed [52] and of triaxially deformed nuclei [53]. It is important to note that this formulation can treat imaginary solutions of the QRPA that may appear in the LQRPA at nonequilibrium HFB states obtained by the CHFb calculations.

The main aim of this paper is to propose a new method to efficiently evaluate the collective inertia used in the WKB approximation for spontaneous fission and in the vibrational kinetic terms in the collective Hamiltonian method. The method is based on the CHFb + LQRPA with the Skyrme EDF. We employ the PQ representation of the FAM to efficiently solve the LQRPA equations. We extend a contour integration approach of the FAM proposed in Ref. [38] to compute the collective inertia associated with the most collective local normal mode in the LQRPA.

This paper is organized as follows. Section II briefly summarizes the formulations of the collective inertia in ATDHFB with the cranking approximation and in the LQRPA. In Sec. III, we explain the formulation of the CHFb + LQRPA with the FAM to calculate the collective inertia. In Sec. IV, we present the results of the collective inertia along a mass-symmetric fission path in ^{240}Pu and ^{256}Fm and compare our results with those of the cranking approximation. Conclusions are given in Sec. V.

II. COLLECTIVE INERTIA WITH ENERGY DENSITY FUNCTIONAL

A. Adiabatic time-dependent Hartree-Fock-Bogoliubov method

We give a brief explanation for the collective inertia in ATDHFB. For details, we refer to Refs. [11,15,16,19].

In ATDHFB, the collective motion of the system is assumed to be described by a set of a few collective coordinates s_i and the conjugate momenta. The collective coordinates are defined as $s_i = \langle \phi(s) | \hat{s}_i | \phi(s) \rangle$, where \hat{s}_i are generators driving the collective motion. In practice, the collective subspace $|\phi(s)\rangle$ is determined by the CHFb calculation with the constraint on s_i . Most applications take \hat{s}_i as one-body operators of multipole moments. The ATDHFB relies on the assumption that the collective velocities of the system denoted by the time derivative of the collective coordinates \dot{s}_i are slow enough to make adiabatic assumption valid. The expression of the collective inertia tensor in ATDHFB is given by

$$\mathcal{M}_{ij} = \frac{i}{2\dot{s}_i\dot{s}_j} \text{Tr}(F^{i*}Z^j - F^iZ^{j*}). \quad (1)$$

The matrix Z involves time-odd fields associated with time-odd density matrices. A standard method to determine the matrix Z requires a solution of the QRPA equation. The matrix F is evaluated by

$$\frac{F^i}{\dot{s}_i} = U^\dagger \frac{\partial \rho}{\partial s_i} V^* + U^\dagger \frac{\partial \kappa}{\partial s_i} U^* - V^\dagger \frac{\partial \rho^*}{\partial s_i} U^* - V^\dagger \frac{\partial \kappa^*}{\partial s_i} V^*, \quad (2)$$

where U and V are the Bogoliubov transformation matrices and ρ and κ are the density matrix and pairing tensor, respectively. This expression includes derivatives of density matrices with respect to the collective coordinates.

1. Cranking approximation

The cranking approximation neglects the time-odd fields in the collective inertia (1). In this case, the matrix Z^i can be simply written in terms of F^i and the quasiparticle energies. The collective inertia tensor of the cranking approximation

then reads in the quasiparticle basis

$$\mathcal{M}_{ij}^C = \frac{1}{2\dot{s}_i\dot{s}_j} \sum_{\mu\nu} \frac{(F_{\mu\nu}^{ik} F_{\mu\nu}^j + F_{\mu\nu}^i F_{\mu\nu}^{j*})}{E_\mu + E_\nu}, \quad (3)$$

where E_μ and E_ν are one-quasiparticle energies defined with respect to the constrained Hamiltonian of the form of Eq. (7) and the CHFB state $|\phi(s)\rangle$ of Eq. (6).

2. Perturbative cranking approximation

Further approximation leads to the so-called perturbative cranking approximation, where the derivatives of the densities with respect to the collective coordinates in Eq. (2) are not explicitly evaluated but are obtained in a perturbative manner. The expression of the collective inertia in the perturbative cranking approximation is given as

$$\mathcal{M}^{\text{PC}} = \frac{1}{2}[M^{(1)}]^{-1}M^{(3)}[M^{(1)}]^{-1}, \quad (4)$$

where the n th energy-weighted moment $M^{(n)}$ is given as

$$M_{ij}^{(n)} = \sum_{\mu<\nu} \frac{\langle\phi(s)|\hat{s}_i|\mu\nu\rangle\langle\mu\nu|\hat{s}_j^\dagger|\phi(s)\rangle}{(E_\mu + E_\nu)^n}, \quad (5)$$

where $|\mu\nu\rangle$ are two-quasiparticle states based on the CHFB state $|\phi(s)\rangle$.

B. Constrained Hartree–Fock–Bogoliubov + local quasiparticle random-phase approximation

Another method to evaluate the collective inertia is the CHFB + LQRPA [26] derived from the ASCC method [25]. Suppose that a set of N collective coordinates q_i ($i = 1, \dots, N$) self-consistently determined with the ASCC method can be mapped to a set of N collective variables s_m ($m = 1, \dots, N$) through a one-to-one correspondence between them. In addition, we assume that the ASCC collective subspace can be approximated by the one obtained with the CHFB calculation with a given set of constraining operators \hat{s}_m . The CHFB equation is given by

$$\delta\langle\phi(s)|\hat{H}_M|\phi(s)\rangle = 0, \quad (6)$$

with the constrained Hamiltonian

$$\hat{H}_M = \hat{H} - \sum_{\tau=n,p} \lambda_\tau \hat{N}_\tau - \sum_m \lambda_m \hat{s}_m, \quad (7)$$

where $\lambda_{n,p}$ denote the Fermi energies for neutrons and protons to constrain the average neutron and proton numbers $\langle\phi(s)|\hat{N}_\tau|\phi(s)\rangle$ ($\tau = n, p$) and λ_m are the Lagrange multipliers of constraining $\langle\phi(s)|\hat{s}_m|\phi(s)\rangle = s_m$. The energy minimization (6) leads to the CHFB state $|\phi(s)\rangle$ and the collective potential $V(s) = \langle\phi(s)|\hat{H}|\phi(s)\rangle$. At each CHFB state $|\phi(s)\rangle$, the LQRPA equations,

$$\delta\langle\phi(s)|[\hat{H}_M, \hat{Q}_i(s)] - \frac{1}{i}\hat{P}_i(s)|\phi(s)\rangle = 0, \quad (8)$$

$$\delta\langle\phi(s)|\left[\hat{H}_M, \frac{1}{i}\hat{P}_i(s)\right] - \Omega_i^2(s)\hat{Q}_i(s)|\phi(s)\rangle = 0, \quad (9)$$

are solved to determine $\hat{Q}_i(s)$ and $\hat{P}_i(s)$ that are local generators of collective coordinates and momenta, respectively,

defined at s . They should satisfy the weak canonicity condition (19). Here, the inertial and the curvature tensors are diagonalized to define the local normal mode. Furthermore, in order to fix the arbitrary scale of the collective coordinate q_i , the inertia with respect to q_i is set to be unity, $\mathcal{M}_{ij} = \delta_{ij}$. $\Omega_i^2(s)$ denotes the squared eigenfrequency of the local normal mode. Note that the eigenfrequency of the LQRPA equations can be imaginary [$\Omega_i^2(s) < 0$] at nonequilibrium CHFB states. A criterion for selecting relevant collective LQRPA modes from many LQRPA solutions is given in Ref. [26].

Once relevant LQRPA collective modes are selected, the collective inertia tensor is given as follows. First, the collective kinetic energy is expressed as

$$T = \frac{1}{2} \sum_i \dot{q}_i^2 = \frac{1}{2} \sum_{mn} \mathcal{M}_{mn}(s) \dot{s}_m \dot{s}_n, \quad (10)$$

where collective inertia tensor $\mathcal{M}_{mn}(s)$ is defined by the transformation of the collective coordinates q_i to the collective variables s ,

$$\mathcal{M}_{mn}(s) \equiv \sum_{i,j} \frac{\partial q_i}{\partial s_m} \mathcal{M}_{ij} \frac{\partial q_j}{\partial s_n} = \sum_i \frac{\partial q_i}{\partial s_m} \frac{\partial q_i}{\partial s_n}. \quad (11)$$

Second, the partial derivatives in Eq. (11) are evaluated by using the local generator $\hat{P}_i(s)$ of the LQRPA solution as

$$\begin{aligned} \frac{\partial s_m}{\partial q_i} &= \frac{\partial}{\partial q_i} \langle\phi(s)|\hat{s}_m|\phi(s)\rangle \\ &= \langle\phi(s)|\left[\hat{s}_m, \frac{1}{i}\hat{P}_i(s)\right]|\phi(s)\rangle, \end{aligned} \quad (12)$$

which is calculable without numerical derivatives.

III. FINITE-AMPLITUDE METHOD FOR COLLECTIVE INERTIA

In this work, we use the LQRPA method to evaluate the collective inertia along a fission path. Since it is computationally hard to solve the LQRPA equations for deformed nuclear shapes with the Skyrme EDF, we employ the FAM to efficiently solve the LQRPA equations. In this section, we explain our method to obtain the expression of the collective inertia based on the FAM and LQRPA.

A. Finite-amplitude method

Here, the FAM is recapitulated. The details of its derivation can be found in Refs. [32,34]. The FAM equations can be expressed in the quasiparticle basis as

$$(E_\mu + E_\nu - \omega)X_{\mu\nu}(\omega) + \delta H_{\mu\nu}^{20}(\omega) = -F_{\mu\nu}^{20}, \quad (13a)$$

$$(E_\mu + E_\nu + \omega)Y_{\mu\nu}(\omega) + \delta H_{\mu\nu}^{02}(\omega) = -F_{\mu\nu}^{02}, \quad (13b)$$

where $X_{\mu\nu}(\omega)$ and $Y_{\mu\nu}(\omega)$ are the FAM amplitudes at a given frequency ω , and $\delta H_{\mu\nu}^{20(02)}$ and $F_{\mu\nu}^{20(02)}$ are two-quasiparticle components of one-body induced field $\delta\hat{H}$ and an external field \hat{F} , respectively. The FAM equations (13) are iteratively solved at each ω until converged X and Y amplitudes are obtained. Complex frequency ω is usually used with the imaginary part corresponding to a smearing width. Only one-body

quantities (induced densities and induced fields) are necessary to solve the FAM equations.

The FAM strength function is given from converged X and Y amplitudes as

$$S(\hat{F}, \omega) = \sum_{\mu < \nu} [F_{\mu\nu}^{20*} X_{\mu\nu}(\omega) + F_{\mu\nu}^{02*} Y_{\mu\nu}(\omega)]. \quad (14)$$

Taking the frequency ω real and positive, the transition strength distribution is given as

$$\frac{dB(\hat{F}, \omega)}{d\omega} \equiv \sum_{i(\Omega_i > 0)} |\langle i | \hat{F} | 0 \rangle|^2 \delta(\omega - \Omega_i) = -\frac{1}{\pi} \text{Im} S(\hat{F}, \omega), \quad (15)$$

where $|0\rangle$ is the QRPA vacuum and $|i\rangle \equiv \hat{O}_i^\dagger |0\rangle$ is a state of the QRPA normal mode of excitation with the eigenfrequency Ω_i .

The relation between the FAM strength function (14) and the QRPA transition strength $|\langle i | \hat{F} | 0 \rangle|^2$ between the ground state and a QRPA eigenstate $|i\rangle$ is given as [38]

$$S(\hat{F}, \omega) = - \sum_{i(\Omega_i > 0)} \left(\frac{|\langle i | \hat{F} | 0 \rangle|^2}{\Omega_i - \omega} + \frac{|\langle 0 | \hat{F} | i \rangle|^2}{\Omega_i + \omega} \right). \quad (16)$$

B. Finite-amplitude method in the momentum-coordinate representation

In Ref. [47], the FAM in the PQ representation of the QRPA was formulated to investigate the NG modes and the Thouless–Valatin inertia of the NG modes. In this section, we summarize the formulation of the FAM in the PQ representation.

In the PQ representation of the QRPA, the coordinate and the conjugate momentum operators, \hat{Q}_i and \hat{P}_i , which are both Hermitian, are constructed from the QRPA phonon operators ($\hat{O}_i, \hat{O}_i^\dagger$) as

$$\hat{Q}_i = \sqrt{\frac{1}{2M_i\Omega_i}} (\hat{O}_i + \hat{O}_i^\dagger), \quad (17)$$

$$\hat{P}_i = \frac{1}{i} \sqrt{\frac{M_i\Omega_i}{2}} (\hat{O}_i - \hat{O}_i^\dagger), \quad (18)$$

where M_i is the inertia parameter. The operators \hat{Q}_i and \hat{P}_i fulfill the following commutation relations:

$$\begin{aligned} \langle 0 | [\hat{Q}_i, \hat{P}_j] | 0 \rangle &= i\delta_{ij}, \\ \langle 0 | [\hat{Q}_i, \hat{Q}_j] | 0 \rangle &= \langle 0 | [\hat{P}_i, \hat{P}_j] | 0 \rangle = 0, \end{aligned} \quad (19)$$

which guarantee the orthogonality among different normal modes, however, their scale is still arbitrary as $(\alpha\hat{Q}_i, \alpha^{-1}\hat{P}_i)$. In the present study, this scale is fixed by imposing the additional condition, $M_i = 1$. Then, these correspond to solutions of Eqs. (8) and (9).

Using two-quasiparticle components $P_{\mu\nu}^i$ and $Q_{\mu\nu}^i$ of the operators \hat{P}_i and \hat{Q}_i , the FAM X and Y amplitudes are

given as

$$X_{\mu\nu}(\omega) = \sum_i \frac{1}{\omega^2 - \Omega_i^2} [(-i\omega P_{\mu\nu}^i + \Omega_i^2 Q_{\mu\nu}^i) q_i(\hat{F}) + (P_{\mu\nu}^i + i\omega Q_{\mu\nu}^i) p_i(\hat{F})], \quad (20a)$$

$$Y_{\mu\nu}(\omega) = \sum_i \frac{1}{\omega^2 - \Omega_i^2} [(i\omega P_{\mu\nu}^{i*} - \Omega_i^2 Q_{\mu\nu}^{i*}) q_i(\hat{F}) + (-P_{\mu\nu}^{i*} - i\omega Q_{\mu\nu}^{i*}) p_i(\hat{F})], \quad (20b)$$

where $p_i(\hat{F})$ and $q_i(\hat{F})$ are defined as

$$p_i(\hat{F}) \equiv \langle 0 | [\hat{P}_i, \hat{F}] | 0 \rangle = \sum_{\mu < \nu} (P_{\mu\nu}^{i*} F_{\mu\nu}^{20} - P_{\mu\nu}^i F_{\mu\nu}^{02}), \quad (21)$$

$$q_i(\hat{F}) \equiv \langle 0 | [\hat{Q}_i, \hat{F}] | 0 \rangle = \sum_{\mu < \nu} (Q_{\mu\nu}^{i*} F_{\mu\nu}^{20} - Q_{\mu\nu}^i F_{\mu\nu}^{02}). \quad (22)$$

The FAM strength function (14) is then rewritten as

$$\begin{aligned} S(\hat{F}, \omega) &= \sum_{\mu < \nu} [F_{\mu\nu}^{20*} X_{\mu\nu}(\omega) + F_{\mu\nu}^{02*} Y_{\mu\nu}(\omega)] \\ &= \sum_i \frac{1}{\omega^2 - \Omega_i^2} [p_i(\hat{F})^2 + \Omega_i^2 q_i(\hat{F})^2 + \omega r_i(\hat{F})], \end{aligned} \quad (23)$$

with a real quantity

$$r_i(\hat{F}) \equiv i[q_i^*(\hat{F}) p_i(\hat{F}) - q_i(\hat{F}) p_i^*(\hat{F})]. \quad (24)$$

The FAM $X(\omega)$ and $Y(\omega)$ amplitudes (20) and the FAM strength function (23) are defined in the whole complex plane ω except for $\omega = \pm\Omega_i$. They are well defined even with the presence of the NG modes ($\Omega_i^2 = 0$) and the imaginary solutions ($\Omega_i^2 < 0$) which can appear in the LQRPA at nonequilibrium CHF states.

C. Collective inertia with finite-amplitude method plus contour integration technique

For simplicity, in this paper, we assume only one collective coordinate q , and then adopt the isoscalar quadrupole moment $\hat{s} = \hat{Q}_{20} = \sqrt{16\pi/5} \sum_{i=1}^A r_i^2 Y_{20}(\hat{r}_i)$ as the constraint. For the LQRPA calculation, we adopt the same operator for the external field $\hat{F} = \hat{Q}_{20}$. Then, by transforming the scale of the coordinate from q to $s = \langle \phi(s) | \hat{Q}_{20} | \phi(s) \rangle$, the expression of the collective inertia (11) becomes

$$\mathcal{M} \equiv \frac{dq}{ds} \frac{dq}{ds}, \quad (25)$$

with $dq/ds = (ds/dq)^{-1}$ and

$$\begin{aligned} \frac{ds}{dq} &= \langle \phi(s) | \left[\hat{Q}_{20}, \frac{1}{i} \hat{P}_i \right] | \phi(s) \rangle \\ &= ip_i(\hat{Q}_{20}). \end{aligned} \quad (26)$$

We will see below that $p_i(\hat{Q}_{20})$ is pure imaginary, leading to real ds/dq . We select the normal mode i which has the largest value of $|p_i(\hat{Q}_{20})|^2$ among the low-lying eigenmodes.

The remaining task is the calculation of $p_i(\hat{F}) = p_i(\hat{Q}_{20})$ in the FAM. From Eqs. (17) and (18), P^i and Q^i are given in

terms of the forward and backward amplitudes of the QRPA normal modes, X^i and Y^i , as

$$P_{\mu\nu}^i = i\sqrt{\frac{\Omega_i}{2}}(X_{\mu\nu}^i + Y_{\mu\nu}^i), \quad (27)$$

$$Q_{\mu\nu}^i = \sqrt{\frac{1}{2\Omega_i}}(X_{\mu\nu}^i - Y_{\mu\nu}^i). \quad (28)$$

Note that we set $M_i = 1$. When the QRPA matrices are real, we may choose $X_{\mu\nu}^i$ and $Y_{\mu\nu}^i$ real. This leads to real $Q_{\mu\nu}^i$ and pure imaginary $P_{\mu\nu}^i$. In the present case, the external-field operator $\hat{F} = \hat{Q}_{20}$ is Hermitian and their two-quasiparticle components are real, namely, $F^{02} = F^{20*} = F^{20}$. Thus, $q_i(\hat{F}) = 0$ and $p_i(\hat{F}) = -p_i^*(\hat{F})$ (pure imaginary) hold according to Eq. (22). Then, the FAM strength function (23) becomes

$$S(\hat{F}, \omega) = \sum_i \frac{1}{\omega^2 - \Omega_i^2} |p_i(\hat{F})|^2. \quad (29)$$

Since the right-hand side of Eq. (29) has first-order poles at $\omega = \pm\Omega_i$, we obtain the following expression using Cauchy's integral formula,

$$\frac{1}{2\pi i} \oint_{C_i} \omega S(\hat{F}, \omega) d\omega = \frac{1}{2} |p_i(\hat{F})|^2, \quad (30)$$

where the contour circle C_i in the complex energy plane is chosen to encircle only the pole $\omega = \Omega_i$. The strength functions, $S(\hat{F}, \omega)$, at different values of ω are obtained as Eq. (14) with an iterative solution of Eq. (13).

The eigenfrequency Ω_i can be also obtained by combining Eq. (30) with the following contour integration:

$$\frac{1}{2\pi i} \oint_{C_i} S(\hat{F}, \omega) d\omega = \frac{1}{2\Omega_i} |p_i(\hat{F})|^2. \quad (31)$$

The expressions (30) and (31) can be used for both real and pure imaginary eigenfrequencies.

D. Numerical procedure

To prepare the CHFB states along the fission path, we solve the CHFB equations with the two-basis method [54,55], where during iteration the HFB Hamiltonian is diagonalized in a single-particle basis that converges to the eigenstates of the mean-field Hamiltonian, called the Hartree-Fock (HF) basis, and the local densities are constructed in the canonical basis that diagonalizes the density matrix. The single-particle wave functions and fields are represented in a three-dimensional (3D) Cartesian mesh. Nuclear shapes are restricted to have three plane reflection symmetries about the $x = 0$, $y = 0$, and $z = 0$ planes. This reduces the model space to 1/8 of the full box and can be realized by choosing the single-particle wave functions as eigenstates of parity, z signature, and y time simplex [56–59]. This symmetry restriction prevents us from treating asymmetric fission in the present study. We use a numerical box of 13.2 fm for x and y directions and 19.6 fm for z direction in $x > 0$, $y > 0$, and $z > 0$ in order to express prolately deformed fissioning shapes, discretized with the mesh size of 0.8 fm for all directions. The

number of mesh points then becomes $16 \times 16 \times 24 = 6144$. The single-particle basis consists of 2460 neutron and 1840 proton HF-basis states to achieve the maximum quasiparticle energy of $E_{\text{QP}}^{\text{max}} \approx 60$ MeV for both neutrons and protons in ^{240}Pu and ^{256}Fm . Constrained quantities are the isoscalar quadrupole moment $Q_{20} = \langle \hat{Q}_{20} \rangle$ with $\langle \hat{Q}_{22} \rangle = 0$, keeping axially symmetric shapes. The symmetry restriction automatically constrains the position of the center of mass, and $\langle xy \rangle = \langle yz \rangle = \langle zx \rangle = 0$. The other even-multipole moments are not constrained, and their values are optimized to minimize the total energy, while the expectation values of all odd-multipole moments are kept to be zero due to the plane reflection symmetries of nuclear shapes. We used the SkM* EDF [60] and the contact volume pairing with a pairing window of 20 MeV above and below the Fermi energy in the HF basis described in Refs. [56,58] to avoid divergence in the pairing energy. The pairing strengths are adjusted separately for neutrons and protons in order to reproduce the empirical pairing gaps in ^{240}Pu or in ^{256}Fm .

We have extended our 3D FAM-QRPA code developed in Ref. [46] to perform FAM calculations at CHFB states and the FAM-QRPA with the contour integration. We include in the FAM the full quasiparticle basis included in the CHFB calculations to satisfy full self-consistency between the CHFB and LQRPA calculations. We employ the modified Broyden method [61] for iteratively solving the FAM equations.

To obtain the quantity $|p_i(\hat{F})|^2$ by the contour integration (30), it is necessary to know in advance an approximate position of each QRPA pole $\omega = \Omega_i$ in the complex energy plane for determining an appropriate contour C_i . The QRPA poles are expected to appear as sharp peaks in the FAM strength distribution. Therefore, we first calculate the FAM strength distribution (15) in the low-lying states with $\omega^2 < 16$ MeV². For each pole, we calculate $|p_i(\hat{F})|^2$ and adopt the most collective mode with the largest value of $|p_i(\hat{F})|^2$. A detail of our procedure of selecting the most collective mode in the FAM is given in the Appendix. For the integration contour, we use a circle centered at the estimated peak frequency. The radius is 0.05 MeV for real solutions, and 0.1 MeV for an imaginary solution. If there are other poles close to the present pole, we use a circle with even smaller radius. The number of discretization points along the circle is twelve for real and eight for imaginary solutions.

We perform numerical calculations of the FAM with a hybrid parallel scheme. The MPI parallelization is adopted for calculation of $S(\hat{F}, \omega)$ at different ω points. The FAM iterative solution of Eq. (13) at each ω is performed by using the OpenMP parallel calculation. It takes about 160 core hours on Oakforest-PACS for the FAM contour integration for a real solution at one deformation point with the present model space.

Before we proceed, we would like to discuss the convergence property of the collective inertia with respect to the size of the model space included in the ground state. To check the convergence property, we calculated the collective inertia with different numbers of HF-basis states corresponding to different $E_{\text{QP}}^{\text{max}}$ values in the ground state. Figure 1 shows the collective inertia as a function of neutron $E_{\text{QP}}^{\text{max}}$ (nearly equal to proton $E_{\text{QP}}^{\text{max}}$) divided by that calculated with neutron

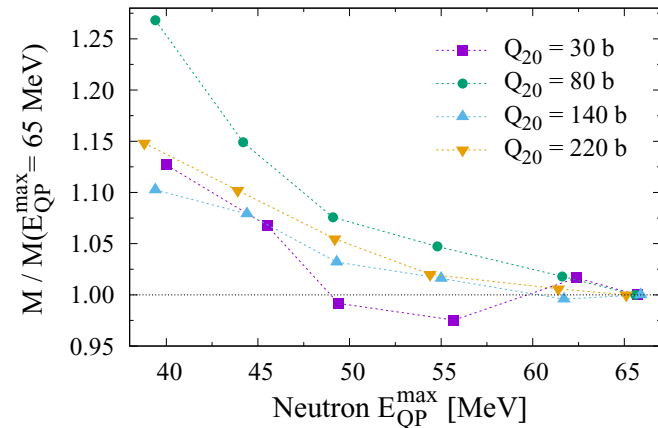


FIG. 1. Collective inertia as a function of E_{QP}^{\max} for neutrons divided by that with neutron $E_{QP}^{\max} \approx 65$ MeV for four different deformation points in ^{240}Pu . Included neutron HF-basis states are 1200, 1440, 1632, 1998, 2460, and 2700 for $E_{QP}^{\max} \approx 40, 45, 50, 55, 60,$ and 65 MeV, respectively.

$E_{QP}^{\max} \approx 65$ MeV as a reference value for four various deformation points in ^{240}Pu . We find that the model space with neutron $E_{QP}^{\max} \geq 55$ MeV gives a good convergence within about less than 5% to the value with $E_{QP}^{\max} \approx 65$ MeV for the four various deformation points. Therefore, as mentioned above, we include 2460 neutron and 1840 proton HF-basis states corresponding to $E_{QP}^{\max} \approx 60$ MeV in our calculations. Note again that we do not introduce in the FAM calculations the additional two-quasiparticle energy cutoff, which has been usually employed to reduce the dimension of the QRPA matrix.

IV. RESULTS

Mass distributions of fission fragments measured in low-energy fission show a sudden change from asymmetric to symmetric mass distributions when the neutron number changes. A well-known example is Fm isotopes, where ^{256}Fm shows an asymmetric mass distribution, while ^{258}Fm shows that the main component of fission fragments is a symmetric one [62,63]. Even more complicated multimode or multichannel fission has been observed and analyzed in the total-kinetic-energy distributions of fission fragments in actinides [64,65]. In EDF-based studies, the fission modes depend on the potential landscape and the collective inertia. Since, so far, most of studies are focused on the potential landscape, we aim at investigating effects of the collective inertia. In this section, we take ^{240}Pu and ^{256}Fm as examples to show the importance of dynamical residual effects on the inertia. Although, in this paper, the calculation is performed only along the symmetric fission path, we show that the residual effect on the inertia may hinder the symmetric fission probability.

A. Collective inertia along a symmetric fission path in ^{240}Pu

Figure 2(a) shows the collective potential energy as a function of expectation value of quadrupole moment Q_{20} in

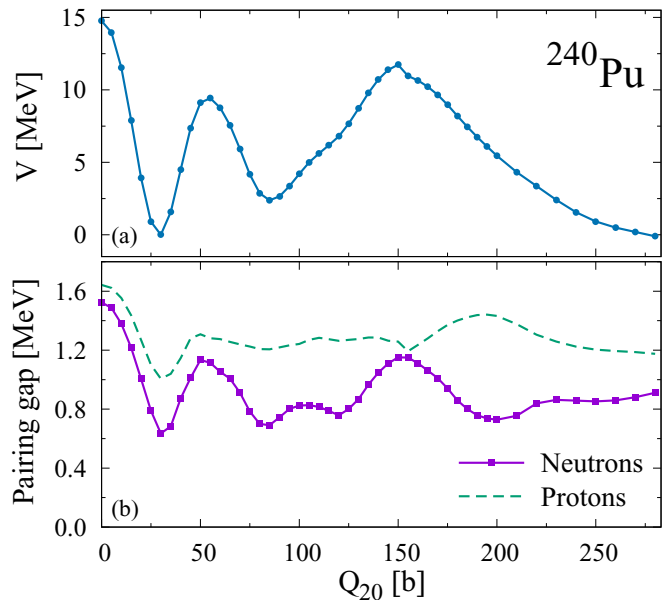


FIG. 2. (a) Potential energy (b) pairing gaps for neutrons (solid line) and protons (dashed line) as a function of quadrupole moment Q_{20} in units of barns in ^{240}Pu .

units of barns (b) along a symmetric fission path in ^{240}Pu obtained from the CHFB calculation. The ground state of ^{240}Pu is found at $Q_{20} \approx 30$ b. The first fission barrier, the fission isomer (local minimum), and the second fission barrier are obtained at $Q_{20} \approx 55$ b, $Q_{20} \approx 85$ b, and $Q_{20} \approx 150$ b, respectively. We would like to note that the heights of the first and second fission barriers would become lower if we could include triaxial deformation for the first fission barrier and octupole deformation for the second fission barrier [66,67]. Neutron and proton pairing gaps are shown along the fission path in Fig. 2(b). The neutron pairing gap becomes larger at the regions near the fission barriers and smaller near the ground state and fission isomer. The proton pairing gap shows a moderate behavior because of the difference between neutron and proton single-particle structures. It is known that transition strengths of low-lying modes are affected by the strength of pairing correlations.

Figure 3(a) shows the collective inertia obtained with the present FAM-QRPA calculation by the filled-square solid line. This shows two prominent peaks at $Q_{20} \approx 25$ b and $Q_{20} \approx 80$ b and a sudden change near these peaks. These states closely correspond to the ground state and the fission isomer observed in Fig. 2(a) and to the states where pairing becomes weak in Fig. 2(b). For comparison, we add in Fig. 3(a) the collective inertia obtained by the perturbative cranking approximation. It is clearly shown that the FAM-QRPA inertia is larger than the perturbative cranking inertia. We emphasize this point in Fig. 3(b), showing that the ratio of the FAM-QRPA inertia to the perturbative cranking inertia always exceeds unity, except at $Q_{20} = 60$ b. This indicates that the action integral in the WKB approximation will be significantly affected by the increase of the collective inertia near the fission barriers. The behaviors of the two inertias are

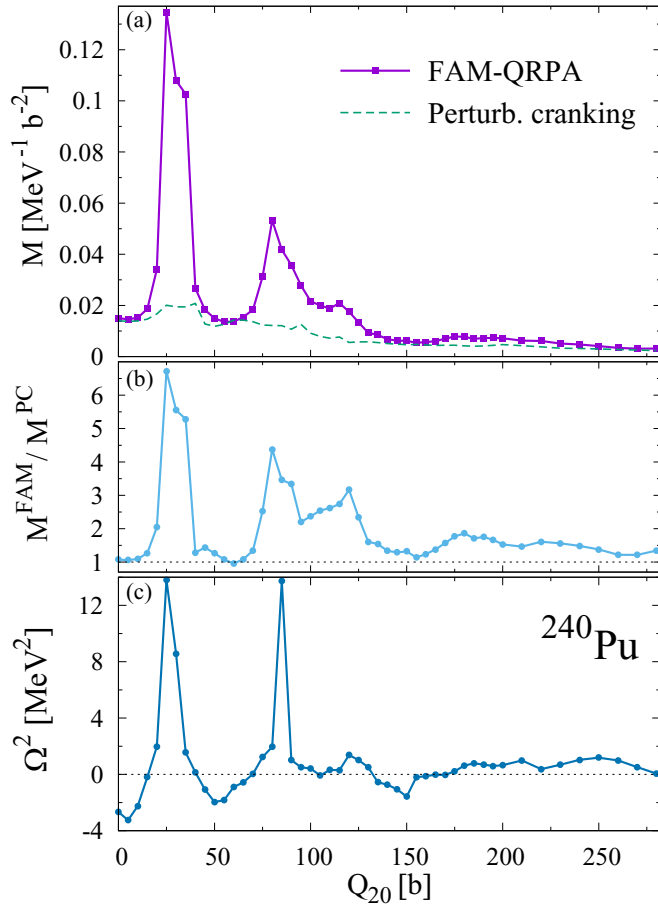


FIG. 3. (a) Collective inertia of the FAM-QRPA calculation shown by the filled-square solid line, and of the perturbative cranking approximation by the dashed line. (b) Ratio of the FAM-QRPA inertia to the perturbative cranking inertia. (c) Squared QRPA eigenfrequency as a function of Q_{20} in ^{240}Pu .

different; the FAM-QRPA inertia shows a strong variation, while the perturbative cranking inertia varies smoothly as Q_{20} increases.

We estimate the action integral in the WKB approximation using the obtained collective inertia and potential along the symmetric fission path. The action integral reads

$$S = \int_{Q_{\text{in}}}^{Q_{\text{out}}} dQ_{20} \sqrt{2\mathcal{M}(Q_{20})[V(Q_{20}) - E_0]}, \quad (32)$$

where Q_{in} and Q_{out} are the classical inner and outer turning points, and E_0 is the HFB ground-state energy. We obtain the action integrals $S_{\text{FAM}} = 82.0$ for the FAM-QRPA inertia and $S_{\text{PC}} = 62.0$ for the perturbative cranking inertia from $Q_{\text{in}} = 30$ b (the ground state) to $Q_{\text{out}} = 270$ b. This difference leads to many orders of magnitude difference in the fission half-life.

Figure 3(c) shows the eigenfrequency squared Ω^2 of the LQRPA solution selected as the most collective mode at each deformation. This represents the curvature of the collective potential, which can indeed become negative at the fission barriers. Larger values of Ω^2 are found at the states with larger values of the collective inertia. As Ω^2 becomes larger, the ratio of the FAM-QRPA inertia to the perturbative cranking inertia

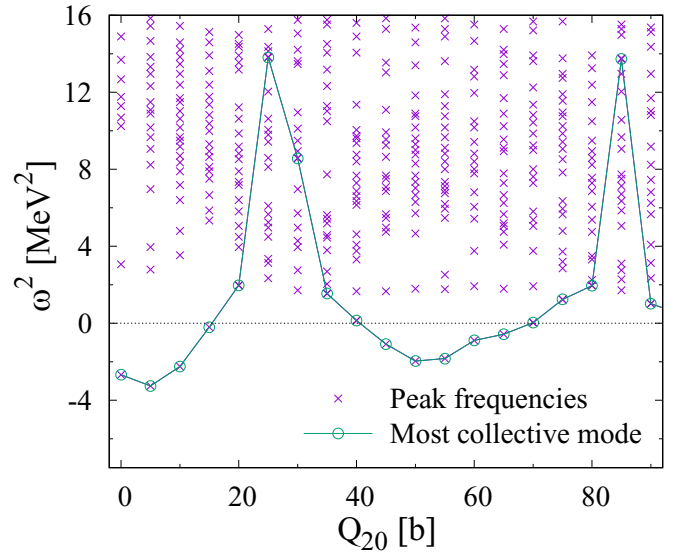
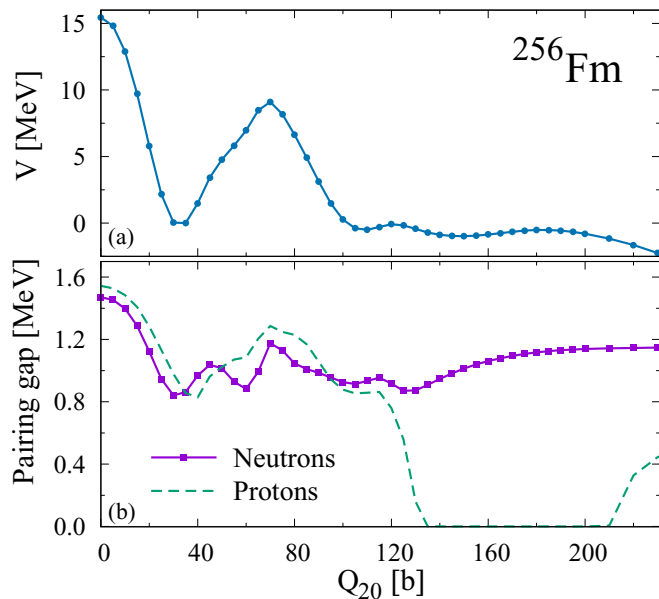


FIG. 4. Squared peak frequencies identified from the FAM strength distribution shown by the crosses as a function of Q_{20} in ^{240}Pu . Eigenfrequency squared of the most collective mode is shown by the open-circle solid line.

becomes larger. When Ω^2 are negative, the ratio is close to unity.

In Fig. 4, we plot the squared peak frequencies identified from the FAM strength distribution in $\omega^2 < 16 \text{ MeV}^2$ as a function of Q_{20} up to the fission isomer ($Q_{20} \leq 90$ b). Note that, because of a finite smearing width ($=0.01 \text{ MeV}$) used in the FAM calculation, the identified peak frequencies may slightly differ from the QRPA eigenfrequencies and may not correspond to all the eigenfrequencies. In the figure, the eigenfrequency squared of the most collective mode that is used in the FAM-QRPA collective inertia is shown by the open-circle solid line. At most regions in Q_{20} , we find that the most collective mode corresponds to the lowest-frequency mode and is well separated from other peaks. On the other hand, around the ground state ($Q_{20} \approx 30$ b) and the fission isomer ($Q_{20} \approx 85$ b), where pairing becomes weak, we find that the most collective mode appears at frequencies close to other peaks, or at higher frequencies. The increase of the FAM-QRPA inertia near the ground and the fission isomer states is due to decrease of the quadrupole collectivity which leads to decrease in $|p_i(\dot{Q}_{20})|^2$. In fact, near the ground state, we find that the character of the lowest frequency mode changes from the quadrupole vibration to the pair vibration.

It is known that QRPA eigenmodes that possess pair-vibrational character tend to appear in low-frequency regions when pairing becomes weak. We analyze the character of the lowest-frequency mode at $\omega \approx 1.5 \text{ MeV}$ at $Q_{20} = 25, 30,$ and 35 b by using the FAM calculation with the pair-vibrational field as an external field. The lowest-frequency modes at $Q_{20} = 25, 30,$ and 35 b have a strong neutron pair-vibrational character and approximately satisfy the relation $\Omega \approx 2\Delta_n$, where Δ_n denotes the neutron pairing gap. The lowest-frequency modes at $Q_{20} = 25$ and 30 b are not the most

FIG. 5. Same as Fig. 2, but for ^{256}Fm .

collective in the quadrupole Q_{20} nature. We also confirm this by calculating the collective inertia for those lowest modes.

For the lowest mode, the collective inertia would be $\mathcal{M} = 0.190 \text{ MeV}^{-1}\text{b}^{-2}$ at $Q_{20} = 25 \text{ b}$ and $\mathcal{M} = 1.02 \text{ MeV}^{-1}\text{b}^{-2}$ at $Q_{20} = 30 \text{ b}$. These values are significantly larger than the values shown in Fig. 3(a), indicating the character change of the lowest mode from the quadrupole vibration to the neutron pair vibration. We note that some EDF-based studies explicitly take pairing fluctuations as other collective variables and show the importance of couplings between shape and pairing degrees of freedom in spontaneous fission [68,69] and the collective Hamiltonian method [70]. It will be a future work to take pairing fluctuations as other collective variables in the CHFB + LQRPA method.

B. Comparison between the FAM-QRPA and nonperturbative cranking inertias in ^{256}Fm

The aim of taking the ^{256}Fm case is to compare the FAM-QRPA collective inertia with that of the nonperturbative cranking approximation by Baran *et al.* in Ref. [11]. In ^{256}Fm , it is known that reflection-symmetric and reflection-asymmetric fission paths bifurcate at $Q_{20} \approx 130 \text{ b}$ [71–73]. In Ref. [11], the collective inertia was calculated along a reflection-symmetric fission path in $Q_{20} < 130 \text{ b}$ and along a reflection-asymmetric fission path in $Q_{20} > 130 \text{ b}$. As we do not include reflection-asymmetric fission paths, we compare the FAM-QRPA collective inertia with that in Ref. [11] along the reflection-symmetric fission path in $Q_{20} \leq 130 \text{ b}$.

First, we show in Fig. 5 the potential and pairing gaps along an axial and reflection-symmetric fission path as a function of Q_{20} . The structure of a fission isomer at $Q_{20} \approx 110 \text{ b}$ almost vanishes due to low second fission barrier height of about 0.4 MeV. The proton pairing vanishes in $Q_{20} \geq 130 \text{ b}$. These properties are consistent with previous EDF studies [11,71–73].

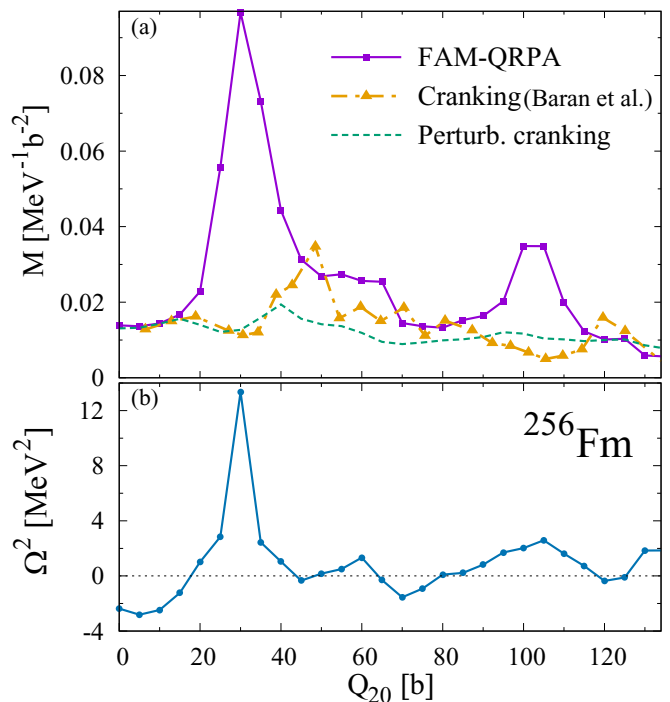


FIG. 6. (a) Comparison between the FAM-QRPA inertia (filled-square solid line), the nonperturbative cranking inertia taken from Baran *et al.* [11] (filled-triangle dot-dashed line), and the perturbative cranking inertia (dashed line), and (b) squared QRPA eigenfrequency as a function of Q_{20} along a symmetric fission path in ^{256}Fm .

Figure 6(a) shows the FAM-QRPA collective inertia as a function of Q_{20} . Two peaks in the FAM-QRPA inertia are clearly seen at the ground state ($Q_{20} \approx 30 \text{ b}$) and fission isomer ($Q_{20} \approx 105 \text{ b}$), which is similar to the case of ^{240}Pu . In this figure, we compare the FAM-QRPA inertia with the inertia of the nonperturbative cranking approximation [11], as well as the perturbative cranking one. We should note that the model space, the pairing functional, and so on, adopted in the present study are different from those in Ref. [11]. The FAM-QRPA inertia and the nonperturbative cranking inertia vary significantly as Q_{20} changes, compared with a smooth behavior of the perturbative cranking inertia. We find two significant differences between the FAM-QRPA inertia and the nonperturbative cranking inertia. One is the magnitude of the collective inertia; the FAM-QRPA collective inertia is significantly larger than the nonperturbative cranking one at most deformation points. Similar values are obtained near the top of the fission barrier at $Q_{20} \approx 70 \text{ b}$ and near the bifurcation at $Q_{20} \approx 130 \text{ b}$. The other difference is the position of peaks in Q_{20} in the collective inertia. The FAM-QRPA inertia peaks at slightly smaller Q_{20} than the cranking one does. These significant differences are, at least partially, due to the residual time-odd fields neglected in the cranking approximation.

Figure 6(b) shows the squared QRPA eigenfrequency obtained by the FAM-QRPA. The peak structure of the squared QRPA eigenfrequency is similar to that of the collective inertia, which is also seen in the ^{240}Pu case. This suggests that a structure change of the lowest frequency mode affects the collective inertia in ^{256}Fm , analogous to the case of ^{240}Pu .

V. CONCLUSION

We have developed a feasible method of calculating the collective inertia based on the CHF + LQRPA method with the Skyrme EDF. This method includes time-odd components of dynamical residual effects to the collective inertia in a self-consistent way. We efficiently calculated the QRPA transition strengths by using the FAM and contour integration technique. We applied this method of evaluating the collective inertia along a symmetric fission path of ^{240}Pu and ^{256}Fm . The results show that the dynamical residual effects significantly affect the collective inertia and result in an enhancement of the collective inertia compared with the perturbative cranking one. The enhancement depends strongly on the deformation of the states. This is a consequence of microscopic dynamical effects. In the case of ^{256}Fm , we also compare the FAM-QRPA inertia with the nonperturbative cranking collective inertia in Ref. [11]. Both collective inertias show peak structures, which are not seen in the perturbative cranking inertia. The values of the deformation at the peaks in the inertia are different. The FAM-QRPA inertia takes much larger values than nonperturbative one around the potential minima.

For future works, it is desirable to lift the symmetry restriction and to study collective inertia along the asymmetric fission paths. We also plan to extend the present method to include two or more collective variables for constructing collective inertia tensors such as a simultaneous treatment of quadrupole and octupole moments and pairing fluctuations along multiple fission paths. Systematic study of the dynamical residual effects on collective inertia in fission in actinide and transactinide nuclei will be important not only for deeper understanding of fission but also for reliable evaluation of fission half-lives in r -process nucleosynthesis. The present method can be also used to describe large-amplitude collective dynamics with the collective Hamiltonian method. It would be interesting to compare the FAM-QRPA inertia with the full ATDHFB inertia [44].

ACKNOWLEDGMENTS

The work was supported in part by QR Program of Kyushu University, by JSPS KAKENHI Grants No. JP18H01209, No. JP19H05142, and No. JP20K03964, and by JSPS-NSFC Bilateral Program for Joint Research Project on ‘‘Nuclear mass and life for unravelling mysteries of r -process.’’ Numerical calculations were performed in part using the COMA (PACS-IX) and Oakforest-PACS Systems through the Multi-disciplinary Cooperative Research Program of the Center for Computational Sciences, University of Tsukuba.

APPENDIX: SELECTION OF THE MOST COLLECTIVE MODE

We explain our procedure of selecting the most collective QRPA eigenmode to calculate the collective inertia. First, we perform the FAM calculation with an isoscalar quadrupole external field \hat{Q}_{20} and a complex frequency $\omega = \omega_R + i\omega_I$ along

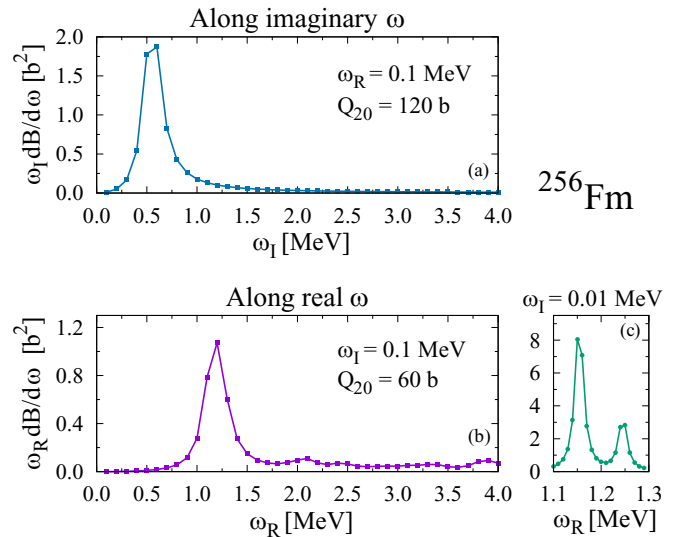


FIG. 7. Example of the strength distribution along the imaginary axis at (a) $Q_{20} = 120$ b and real axis at (b) $Q_{20} = 60$ b in ^{256}Fm . These strength distributions are calculated at each 0.1 MeV with a smearing width of 0.1 MeV. (c) A smaller smearing width of 0.01 MeV at each 0.01 MeV in ω_R is used for the same case as panel (b).

the imaginary and real ω axes to obtain the FAM strength distribution. For the FAM calculation along the imaginary ω axis, ω_R has a role of a smearing width.

Next, we search sharp peaks in the FAM strength distribution, which appear at approximate positions of the QRPA poles, $\omega = \Omega_i$, in $0 \leq \omega_R(\omega_I) \leq 4$ MeV along the real (imaginary) axis with a smearing width of $\omega_I(\omega_R) = 0.1$ MeV. An example of peak search from the strength distribution is shown in Fig. 7 at $Q_{20} = 60$ and 120 b in ^{256}Fm . In Fig. 7(a), the strength distribution at $Q_{20} = 120$ b along the imaginary ω axis shows a clear peak with large magnitude, corresponding to a pure imaginary QRPA pole. We found that either single peak with large magnitude or no peak appears in the strength distribution along the imaginary ω axis for the cases considered here. In Fig. 7(b), for the strength distribution at $Q_{20} = 60$ b along the real ω axis, one peak with larger magnitude is found at $\omega_R \approx 1.2$ MeV. However, we found that this peak is resolved as two peaks at $\omega_R = 1.15$ and 1.25 MeV by the FAM calculation with a smaller smearing width of $\omega_I = 0.01$ MeV, which is illustrated in Fig. 7(c). To search sharp peaks in the strength distribution along the real ω axis, we finally used $\omega_I = 0.01$ MeV to determine approximate positions of the QRPA poles. Note that with $\omega_I = 0.01$ MeV we cannot resolve multiple peaks within about 0.05 MeV in frequency in the strength distribution.

We take a few peaks from the large peaks identified in the FAM strength distribution along both the imaginary and real ω axes as candidates of the most collective eigenmode. Then, we perform the contour integration (30) to obtain the transition strength for each candidate, and finally adopt the one with the largest value of $|p_i(\hat{Q}_{20})|^2$ as the most collective eigenmode.

- [1] N. Schunck and L. M. Robledo, Microscopic theory of nuclear fission: A review, *Rep. Prog. Phys.* **79**, 116301 (2016).
- [2] A. N. Andreyev, K. Nishio, and K.-H. Schmidt, Nuclear fission: A review of experimental advances and phenomenology, *Rep. Prog. Phys.* **81**, 016301 (2017).
- [3] M. Bender, R. Bernard, G. Bertsch, S. Chiba, J. Dobaczewski, N. Dubray, S. A. Giuliani, K. Hagino, D. Lacroix, Z. Li, P. Magierski, J. Maruhn, W. Nazarewicz, J. Pei, S. Péru, N. Pillet, J. Randrup, D. Regnier, P.-G. Reinhard, L. M. Robledo, W. Ryssens, J. Sadhukhan, G. Scamps, N. Schunck, C. Simenel, J. Skalski, I. Stetcu, P. Stevenson, S. Umar, M. Verriere, D. Vretenar, M. Warda, and S. Åberg, Future of nuclear fission theory, *J. Phys. G* **47**, 113002 (2020).
- [4] Y. T. Oganessian and V. K. Utyonkov, Super-heavy element research, *Rep. Prog. Phys.* **78**, 036301 (2015).
- [5] S. Hofmann, Super-heavy nuclei, *J. Phys. G* **42**, 114001 (2015).
- [6] M. R. Mumpower, R. Surman, G. C. McLaughlin, and A. Aprahamian, The impact of individual nuclear properties on r -process nucleosynthesis, *Prog. Part. Nucl. Phys.* **86**, 86 (2016).
- [7] S. A. Giuliani, G. Martínez-Pinedo, and L. M. Robledo, Fission properties of superheavy nuclei for r -process calculations, *Phys. Rev. C* **97**, 034323 (2018).
- [8] S. A. Giuliani, G. Martínez-Pinedo, M.-R. Wu, and L. M. Robledo, Fission and the r -process nucleosynthesis of translead nuclei in neutron star mergers, *Phys. Rev. C* **102**, 045804 (2020).
- [9] M. Bender, P.-H. Heenen, and P.-G. Reinhard, Self-consistent mean-field models for nuclear structure, *Rev. Mod. Phys.* **75**, 121 (2003).
- [10] T. Nakatsukasa, K. Matsuyanagi, M. Matsuo, and K. Yabana, Time-dependent density-functional description of nuclear dynamics, *Rev. Mod. Phys.* **88**, 045004 (2016).
- [11] A. Baran, J. A. Sheikh, J. Dobaczewski, W. Nazarewicz, and A. Staszczak, Quadrupole collective inertia in nuclear fission: Cranking approximation, *Phys. Rev. C* **84**, 054321 (2011).
- [12] J. Sadhukhan, K. Mazurek, A. Baran, J. Dobaczewski, W. Nazarewicz, and J. A. Sheikh, Spontaneous fission lifetimes from the minimization of self-consistent collective action, *Phys. Rev. C* **88**, 064314 (2013).
- [13] J. Sadhukhan, W. Nazarewicz, and N. Schunck, Microscopic modeling of mass and charge distributions in the spontaneous fission of ^{240}Pu , *Phys. Rev. C* **93**, 011304(R) (2016).
- [14] J. Sadhukhan, C. Zhang, W. Nazarewicz, and N. Schunck, Formation and distribution of fragments in the spontaneous fission of ^{240}Pu , *Phys. Rev. C* **96**, 061301(R) (2017).
- [15] S. A. Giuliani and L. M. Robledo, Non-perturbative collective inertias for fission: A comparative study, *Phys. Lett. B* **787**, 134 (2018).
- [16] M. Baranger and M. Vénérini, An adiabatic time-dependent Hartree-Fock theory of collective motion in finite systems, *Ann. Phys. (NY)* **114**, 123 (1978).
- [17] P. Ring and P. Schuck, *The Nuclear Many-Body Problem* (Springer-Verlag, New York, 1980).
- [18] D. J. Thouless and J. G. Valatin, Time-dependent Hartree-Fock equations and rotational states of nuclei, *Nucl. Phys.* **31**, 211 (1962).
- [19] J. Dobaczewski and J. Skalski, The quadrupole vibrational inertial function in the adiabatic time-dependent Hartree-Fock-Bogolyubov approximation, *Nucl. Phys. A* **369**, 123 (1981).
- [20] J. Libert, M. Girod, and J.-P. Delaroche, Microscopic descriptions of superdeformed bands with the Gogny force: Configuration mixing calculations in the $A \sim 190$ mass region, *Phys. Rev. C* **60**, 054301 (1999).
- [21] L. Próchniak, P. Quentin, D. Samsøen, and J. Libert, A self-consistent approach to the quadrupole dynamics of medium heavy nuclei, *Nucl. Phys. A* **730**, 59 (2004).
- [22] T. Nikšić, Z. P. Li, D. Vretenar, L. Próchniak, J. Meng, and P. Ring, Beyond the relativistic mean-field approximation. III. Collective Hamiltonian in five dimensions, *Phys. Rev. C* **79**, 034303 (2009).
- [23] J.-P. Delaroche, M. Girod, J. Libert, H. Goutte, S. Hilaire, S. Péru, N. Pillet, and G. F. Bertsch, Structure of even-even nuclei using a mapped collective Hamiltonian and the D1S Gogny interaction, *Phys. Rev. C* **81**, 014303 (2010).
- [24] Z. P. Li, T. Nikšić, D. Vretenar, and J. Meng, Microscopic description of spherical to γ -soft shape transitions in Ba and Xe nuclei, *Phys. Rev. C* **81**, 034316 (2010).
- [25] M. Matsuo, T. Nakatsukasa, and K. Matsuyanagi, Adiabatic selfconsistent collective coordinate method for large amplitude collective motion in nuclei with pairing correlations, *Prog. Theor. Phys.* **103**, 959 (2000).
- [26] N. Hinohara, K. Sato, T. Nakatsukasa, M. Matsuo, and K. Matsuyanagi, Microscopic description of large-amplitude shape-mixing dynamics with inertial functions derived in local quasiparticle random-phase approximation, *Phys. Rev. C* **82**, 064313 (2010).
- [27] K. Sato and N. Hinohara, Shape mixing dynamics in the low-lying states of proton-rich Kr isotopes, *Nucl. Phys. A* **849**, 53 (2011).
- [28] N. Hinohara, K. Sato, K. Yoshida, T. Nakatsukasa, M. Matsuo, and K. Matsuyanagi, Shape fluctuations in the ground and excited 0^+ states of $^{30,32,34}\text{Mg}$, *Phys. Rev. C* **84**, 061302(R) (2011).
- [29] K. Sato, N. Hinohara, K. Yoshida, T. Nakatsukasa, M. Matsuo, and K. Matsuyanagi, Shape transition and fluctuations in neutron-rich Cr isotopes around $N = 40$, *Phys. Rev. C* **86**, 024316 (2012).
- [30] N. Hinohara, Z. P. Li, T. Nakatsukasa, T. Nikšić, and D. Vretenar, Effect of time-odd mean fields on inertial parameters of the quadrupole collective Hamiltonian, *Phys. Rev. C* **85**, 024323 (2012).
- [31] K. Yoshida and N. Hinohara, Shape changes and large-amplitude collective dynamics in neutron-rich Cr isotopes, *Phys. Rev. C* **83**, 061302(R) (2011).
- [32] T. Nakatsukasa, T. Inakura, and K. Yabana, Finite amplitude method for the solution of the random-phase approximation, *Phys. Rev. C* **76**, 024318 (2007).
- [33] T. Inakura, T. Nakatsukasa, and K. Yabana, Self-consistent calculation of nuclear photoabsorption cross sections: Finite amplitude method with Skyrme functionals in the three-dimensional real space, *Phys. Rev. C* **80**, 044301 (2009).
- [34] P. Avogadro and T. Nakatsukasa, Finite amplitude method for the quasiparticle random-phase approximation, *Phys. Rev. C* **84**, 014314 (2011).
- [35] T. Inakura, T. Nakatsukasa, and K. Yabana, Emergence of pygmy dipole resonances: Magic numbers and neutron skins, *Phys. Rev. C* **84**, 021302(R) (2011).
- [36] M. Stoitsov, M. Kortelainen, T. Nakatsukasa, C. Losa, and W. Nazarewicz, Monopole strength function of deformed superfluid nuclei, *Phys. Rev. C* **84**, 041305(R) (2011).
- [37] H. Liang, T. Nakatsukasa, Z. Niu, and J. Meng, Feasibility of the finite-amplitude method in covariant density functional theory, *Phys. Rev. C* **87**, 054310 (2013).

- [38] N. Hinohara, M. Kortelainen, and W. Nazarewicz, Low-energy collective modes of deformed superfluid nuclei within the finite-amplitude method, *Phys. Rev. C* **87**, 064309 (2013).
- [39] T. Nikšić, N. Kralj, T. Tutiš, D. Vretenar, and P. Ring, Implementation of the finite amplitude method for the relativistic quasiparticle random-phase approximation, *Phys. Rev. C* **88**, 044327 (2013).
- [40] M. T. Mustonen, T. Shafer, Z. Zenginerler, and J. Engel, Finite-amplitude method for charge-changing transitions in axially deformed nuclei, *Phys. Rev. C* **90**, 024308 (2014).
- [41] J. C. Pei, M. Kortelainen, Y. N. Zhang, and F. R. Xu, Emergent soft monopole modes in weakly bound deformed nuclei, *Phys. Rev. C* **90**, 051304(R) (2014).
- [42] N. Hinohara, M. Kortelainen, W. Nazarewicz, and E. Olsen, Complex-energy approach to sum rules within nuclear density functional theory, *Phys. Rev. C* **91**, 044323 (2015).
- [43] M. Kortelainen, N. Hinohara, and W. Nazarewicz, Multipole modes in deformed nuclei within the finite amplitude method, *Phys. Rev. C* **92**, 051302(R) (2015).
- [44] K. Wen and T. Nakatsukasa, Self-consistent collective coordinate for reaction path and inertial mass, *Phys. Rev. C* **94**, 054618 (2016).
- [45] X. Sun and D. Lu, Implementation of a finite-amplitude method in a relativistic meson-exchange model, *Phys. Rev. C* **96**, 024614 (2017).
- [46] K. Washiyama and T. Nakatsukasa, Multipole modes of excitation in triaxially deformed superfluid nuclei, *Phys. Rev. C* **96**, 041304(R) (2017).
- [47] N. Hinohara, Collective inertia of the Nambu-Goldstone mode from linear response theory, *Phys. Rev. C* **92**, 034321 (2015).
- [48] Y. Nambu, Quasi-particles and gauge invariance in the theory of superconductivity, *Phys. Rev.* **117**, 648 (1960).
- [49] J. Goldstone, Field theories with superconductor solutions, *Nuovo Cimento* **19**, 154 (1961).
- [50] N. Hinohara and W. Nazarewicz, Pairing Nambu-Goldstone Modes within Nuclear Density Functional Theory, *Phys. Rev. Lett.* **116**, 152502 (2016).
- [51] N. Hinohara, Extending pairing energy density functional using pairing rotational moments of inertia, *J. Phys. G* **45**, 024004 (2018).
- [52] K. Petřík and M. Kortelainen, Thouless-Valatin rotational moment of inertia from linear response theory, *Phys. Rev. C* **97**, 034321 (2018).
- [53] K. Washiyama and T. Nakatsukasa, Multipole modes for triaxially deformed superfluid nuclei, *JPS Conf. Proc.* **23**, 013012 (2018).
- [54] B. Gall, P. Bonche, J. Dobaczewski, H. Flocard, and P.-H. Heenen, Superdeformed rotational bands in the mercury region. A cranked Skyrme-Hartree-Fock-Bogoliubov study, *Z. Phys. A: Hadrons Nucl.* **348**, 183 (1994).
- [55] J. Terasaki, P.-H. Heenen, P. Bonche, J. Dobaczewski, and H. Flocard, Superdeformed rotational bands with density dependent pairing interactions, *Nucl. Phys. A* **593**, 1 (1995).
- [56] P. Bonche, H. Flocard, P.-H. Heenen, S. J. Krieger, and M. S. Weiss, Self-consistent study of triaxial deformations: Application to the isotopes of Kr, Sr, Zr and Mo, *Nucl. Phys. A* **443**, 39 (1985).
- [57] P. Bonche, H. Flocard, and P.-H. Heenen, Self-consistent calculation of nuclear rotations: The complete yrast line of ^{24}Mg , *Nucl. Phys. A* **467**, 115 (1987).
- [58] P. Bonche, H. Flocard, and P.-H. Heenen, Solution of the Skyrme HF + BCS equation on a 3D mesh, *Comput. Phys. Commun.* **171**, 49 (2005).
- [59] V. Hellemans, P.-H. Heenen, and M. Bender, Tensor part of the Skyrme energy density functional. III. Time-odd terms at high spin, *Phys. Rev. C* **85**, 014326 (2012).
- [60] J. Bartel, P. Quentin, M. Brack, C. Guet, and H.-B. Håkansson, Towards a better parametrisation of Skyrme-like effective forces: A critical study of the SkM force, *Nucl. Phys. A* **386**, 79 (1982).
- [61] A. Baran, A. Bulgac, M. M. Forbes, G. Hagen, W. Nazarewicz, N. Schunck, and M. V. Stoitsov, Broyden's method in nuclear structure calculations, *Phys. Rev. C* **78**, 014318 (2008).
- [62] K. F. Flynn, E. P. Horwitz, C. A. A. Bloomquist, R. F. Barnes, R. K. Sjoblom, P. R. Fields, and L. E. Glendenin, Distribution of mass in the spontaneous fission of ^{256}Fm , *Phys. Rev. C* **5**, 1725 (1972).
- [63] D. C. Hoffman, J. B. Wilhelmy, J. Weber, W. R. Daniels, E. K. Hulet, R. W. Lougheed, J. H. Landrum, J. F. Wild, and R. J. Dupzyk, 12.3-min ^{256}Cf and 43-min ^{258}Md and systematics of the spontaneous fission properties of heavy nuclides, *Phys. Rev. C* **21**, 972 (1980).
- [64] E. K. Hulet, J. F. Wild, R. J. Dougan, R. W. Lougheed, J. H. Landrum, A. D. Dougan, M. Schädel, R. L. Hahn, P. A. Baisden, C. M. Henderson, R. J. Dupzyk, K. Sümmerer, and G. R. Bethune, Bimodal Symmetric Fission Observed in the Heaviest Elements, *Phys. Rev. Lett.* **56**, 313 (1986).
- [65] U. Brosa, S. Grossmann, and A. Müller, Fission channels in ^{258}Fm , *Z. Phys. A: At. Nucl.* **325**, 241 (1986).
- [66] L. Bonneau, P. Quentin, and D. Samsøen, Fission barriers of heavy nuclei within a microscopic approach, *Eur. Phys. J. A* **21**, 391 (2004).
- [67] B.-N. Lu, E.-G. Zhao, and S.-G. Zhou, Potential energy surfaces of actinide nuclei from a multidimensional constrained covariant density functional theory: Barrier heights and saddle point shapes, *Phys. Rev. C* **85**, 011301(R) (2012).
- [68] J. Sadhukhan, J. Dobaczewski, W. Nazarewicz, J. A. Sheikh, and A. Baran, Pairing-induced speedup of nuclear spontaneous fission, *Phys. Rev. C* **90**, 061304(R) (2014).
- [69] J. Zhao, B.-N. Lu, T. Nikšić, D. Vretenar, and S.-G. Zhou, Multidimensionally-constrained relativistic mean-field study of spontaneous fission: Coupling between shape and pairing degrees of freedom, *Phys. Rev. C* **93**, 044315 (2016).
- [70] J. Xiang, Z. P. Li, T. Nikšić, D. Vretenar, and W. H. Long, Coupling of shape and pairing vibrations in a collective Hamiltonian based on nuclear energy density functionals, *Phys. Rev. C* **101**, 064301 (2020).
- [71] M. Warda, J. L. Egido, L. M. Robledo, and K. Pomorski, Self-consistent calculations of fission barriers in the Fm region, *Phys. Rev. C* **66**, 014310 (2002).
- [72] N. Dubray, H. Goutte, and J.-P. Delaroche, Structure properties of ^{226}Th and $^{256,258,260}\text{Fm}$ fission fragments: Mean-field analysis with the Gogny force, *Phys. Rev. C* **77**, 014310 (2008).
- [73] A. Staszczak, A. Baran, J. Dobaczewski, and W. Nazarewicz, Microscopic description of complex nuclear decay: Multimodal fission, *Phys. Rev. C* **80**, 014309 (2009).